

# Spatial coherence of the thermal electromagnetic field in the vicinity of a dielectric slab

Wah Tung Lau,<sup>1,2</sup> Jung-Tsung Shen,<sup>2</sup> Georgios Veronis,<sup>2</sup> and Shanhui Fan<sup>1,2,\*</sup>  
<sup>1</sup>*Department of Electrical Engineering, Stanford University, Stanford, California 94305, USA*  
<sup>2</sup>*Ginzton Laboratory, Stanford University, Stanford, California 94305, USA*

(Received 19 October 2006; published 10 July 2007)

We present the analytic calculation of the cross-spectral density tensor of a thermally radiative planar dielectric slab in extreme near-field, intermediate near-field, and far-field zones. We show that the spatial coherence of the thermal field exhibits distinct features in these zones. At a given wavelength  $\lambda$ , the coherence length is many orders of magnitude smaller than  $\lambda$  in the extreme near-field zone, and is roughly  $\lambda/2$  in the far-field zone. In the intermediate near-field zone, the coherence length can be much longer than  $\lambda/2$  if the loss is small. The physical origin of the short-ranged spatial coherence in the extreme near-field zone is the spatially fluctuating surface charges at the air-dielectric interface. We also demonstrate that in the intermediate near-field zone, the long-ranged spatial coherence is induced by the waveguide modes of the dielectric slab. When the loss is small, the long-ranged coherence falls off approximately as  $1/\sqrt{x}$ , in contrast to  $1/x$  for a blackbody radiator, where  $x$  refers to displacement parallel to the slab surface.

DOI: [10.1103/PhysRevE.76.016601](https://doi.org/10.1103/PhysRevE.76.016601)

PACS number(s): 42.25.Kb, 05.40.-a, 78.20.-e

## I. INTRODUCTION

An important property of a thermally radiative source is its degree of coherence. In general, the coherence property of such a source is characterized by the cross-spectral density tensor [1]

$$\vec{W}(\mathbf{r}_1, \mathbf{r}_2, \omega) \delta(\omega - \omega') \equiv \langle \vec{E}(\mathbf{r}_1, \omega) \otimes \vec{E}^*(\mathbf{r}_2, \omega') \rangle, \quad (1)$$

at a given frequency  $\omega$ . Here  $\vec{E}(\mathbf{r}, \omega)$  is the spectral Fourier transform of the electric field  $\vec{E}(\mathbf{r}, t)$ . The superscript \* indicates the complex conjugate,  $\otimes$  is the direct-product of two vectors and the brackets  $\langle \cdots \rangle$  denote a thermal ensemble average.

It was recently recognized that the coherence properties of a thermally radiative body can be drastically different from the blackbody radiator in systems such as microcavities [2], photonic crystals [3–8], or in systems exhibiting surface modes [9,10]. Moreover, these changes can occur both in the near- and the far-field zones. In particular, Carminati *et al.* [10] have shown that in the near field of a polaritonic medium, the range of coherence can be larger than that of the far field and is directly related to the propagating surface polariton mode at the interface between the polaritonic medium and air [9,10]. Such long-ranged coherence property has been shown to be useful, for example, in generating coherent thermal radiation in grating structures [11]. Shchegrov *et al.* [12] demonstrated the spectral changes of the energy density  $I(\mathbf{r}, \omega)$  of the electric field in the near- and far-field zones of a semi-infinite bulk polaritonic material in the frequency range that supports surface waves. Also, the coherence property of thermal emission in the far field from a dielectric slab has been investigated [13].

Motivated by these recent developments, here we investigate the spatial coherence of the thermal field in the vicinity of a dielectric slab with finite thickness. In general, one might expect that the waveguide modes in the dielectric slab play an analogous role as the surface waves in the polaritonic media, and thus long-ranged coherence should also be observed in this class of structures. One might further speculate the occurrence of significant differences in the behaviors of the cross-spectral density tensor  $\vec{W}(\mathbf{r}_1, \mathbf{r}_2, \omega)$  at near- and far-field zones, analogous to the spectral changes in the energy density  $I(\mathbf{r}, \omega)$  for semi-infinite media as in Ref. [12]. Our detailed calculations, as shown in this paper, confirm these expectations. Moreover, our calculations reveal three different zones of coherence behavior:

(1) Extreme near-field zone ( $z_0 \ll d$ ), where the spatial coherence length of  $\vec{W}(\mathbf{r}_1, \mathbf{r}_2, \omega)$  is much less than the wavelength  $\lambda$ . Here  $d$  is the  $1/e$  amplitude decay length in air of the evanescent tail associated with the slab guided modes at frequency  $\omega$ ,  $\mathbf{r}_1$  and  $\mathbf{r}_2$  are chosen at the same height  $z_0$  from the dielectric slab, and  $\lambda = 2\pi c/\omega$  is the wavelength in vacuum.

(2) Intermediate near-field zone, where the field shows long-ranged coherence behavior with coherence length larger than  $\lambda/2$  when the loss is small. In this low-loss case, the envelope of the trace of the cross-spectral density tensor decays approximately as  $1/\sqrt{x}$  for large  $x$ , where  $x$  refers to displacement parallel to the slab surface.

(3) Far-field zone ( $z_0 \gg d$ ): in which the coherence length is  $\sim \lambda/2$ . The envelope of the cross-spectral density tensor decays approximately as  $1/x$ .

This paper is organized as follows: In Sec. II we present and develop the formalism to compute the cross-spectral density tensor. We then discuss in Sec. III the results and the physical interpretations. Finally, we present our conclusions in Sec. IV.

## II. FORMALISM

To begin with, we recapitulate the general notions as in Refs. [10,12], and then develop the formalism for the spe-

\*shanhui@stanford.edu

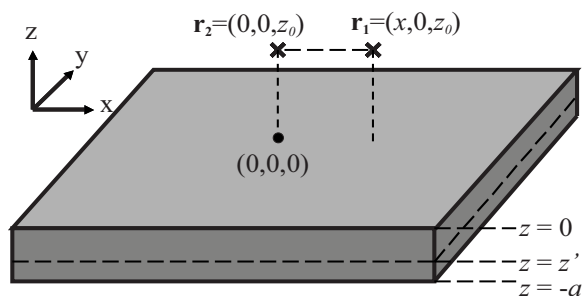


FIG. 1. (Color online) Schematics of the geometry. The gray region represents the dielectric slab. The slab is surrounded by air with unity dielectric constant. It has thickness  $a$  in the  $z$  direction, and extends infinitely in the  $x$  and  $y$  directions.  $\mathbf{r}_1$  and  $\mathbf{r}_2$  are the two observing points above the slab. The coordinates are chosen such that  $\mathbf{r}_1 = (0, 0, z_0)$  and  $\mathbf{r}_2 = (x, 0, z_0)$ . A plane  $z = z'$  with  $-a < z' < 0$  is highlighted by the dashed line. This infinitesimal source plane is to be integrated out to give the contribution to the cross-spectral density tensor between  $\mathbf{r}_1$  and  $\mathbf{r}_2$ .

cific planar slab geometry of interest. We consider the geometry as shown schematically in Fig. 1. The homogeneous lossy dielectric slab has a finite thickness  $a$  in the  $z$  direction ( $-a < z < 0$ ), and extends infinitely in the  $x$  and  $y$  directions. The slab is kept at a uniform temperature  $T$ . From the fluctuation-dissipation theorem [14,15], the presence of loss directly leads to the existence of a fluctuating current density  $\vec{j}(\mathbf{r}, t)$  at any point  $\mathbf{r} = (x, y, z)$  inside the slab. Such fluctuations are a time-stationary random process. The spectral representation  $\vec{j}(\mathbf{r}, \omega)$  is related to its temporal representation by [16]

$$\vec{j}(\mathbf{r}, t) = \int_{-\infty}^{\infty} \frac{d\omega}{2\pi} \vec{j}(\mathbf{r}, \omega) e^{-i\omega t}, \quad (2)$$

and  $\vec{j}(\mathbf{r}, \omega)$  satisfies the fluctuation-dissipation theorem [10],

$$\begin{aligned} \langle \vec{j}(\mathbf{r}, \omega) \otimes \vec{j}^*(\mathbf{r}', \omega') \rangle &= 4\pi\omega\epsilon_0\epsilon''(\omega) \\ &\times \Theta(\omega, T) \delta^3(\mathbf{r} - \mathbf{r}') \delta(\omega - \omega') \vec{I}, \end{aligned} \quad (3)$$

where  $\vec{I}$  is the  $3 \times 3$  identity matrix,  $\Theta(\omega, T) = \hbar\omega / (e^{\hbar\omega/k_B T} - 1)$  is the mean energy above the zero-point energy of a quantum harmonic oscillator in thermal equilibrium at temperature  $T$ , and  $\epsilon''(\omega)$  is the imaginary part of the dielectric constant  $\epsilon(\omega)$ . The form here differs from Ref. [10] by a factor of  $(2\pi)^2$  due to the Fourier transform convention that is used in Eq. (2).

The field radiated into the two half-spaces  $z > 0$  and  $z < -a$  is itself a fluctuating quantity described by a time-stationary random process  $\vec{E}(\mathbf{r}, t)$ . The basic quantity of interest is the second-order coherence of vector fields in the space-time domain [17]

$$\vec{\Gamma}(\mathbf{r}_1, \mathbf{r}_2, \tau) \equiv \langle \vec{E}(\mathbf{r}_1, t) \otimes \vec{E}^*(\mathbf{r}_2, t + \tau) \rangle, \quad (4)$$

which obeys the symmetry property,  $\vec{\Gamma}(\mathbf{r}_1, \mathbf{r}_2, \tau) = \vec{\Gamma}^\dagger(\mathbf{r}_2, \mathbf{r}_1, -\tau)$ , where a dagger denotes the Hermitian conjugate.

According to the Wiener-Khinchine theorem [16,18], we can define the cross-spectral density tensor as

$$\vec{W}(\mathbf{r}_1, \mathbf{r}_2, \omega) = \int_{-\infty}^{\infty} \vec{\Gamma}(\mathbf{r}_1, \mathbf{r}_2, \tau) e^{i\omega\tau} d\tau, \quad (5)$$

$$\vec{\Gamma}(\mathbf{r}_1, \mathbf{r}_2, \tau) = \frac{1}{2\pi} \int_{-\infty}^{\infty} \vec{W}(\mathbf{r}_1, \mathbf{r}_2, \omega) e^{-i\omega\tau} d\omega. \quad (6)$$

It then follows that

$$\vec{W}(\mathbf{r}_1, \mathbf{r}_2, \omega) \delta(\omega - \omega') = \langle \vec{E}(\mathbf{r}_1, \omega) \otimes \vec{E}^*(\mathbf{r}_2, \omega') \rangle.$$

Due to mirror symmetry of our system, we only focus in the region  $z > 0$  hereafter. The electric field at a given point in the half-space  $z > 0$  is given by

$$\vec{E}(\mathbf{r}, \omega) = i\mu_0\omega \int_V \vec{G}(\mathbf{r}, \mathbf{r}', \omega) \vec{j}(\mathbf{r}', \omega) d^3\mathbf{r}', \quad (7)$$

where the integration is performed over the volume  $V$  of the slab.  $\vec{j}(\mathbf{r}', \omega)$  again is the spectral representation of the random current density, and  $\vec{G}(\mathbf{r}, \mathbf{r}', \omega)$  is the Green dyadic of the considered geometry.

Inserting Eq. (7) into Eq. (1), we obtain

$$\begin{aligned} \vec{W}(\mathbf{r}_1, \mathbf{r}_2, \omega) \delta(\omega - \omega') &= \omega^2 \mu_0^2 \int_V d^3\mathbf{r}' \int_V d^3\mathbf{r}'' \langle [\vec{G}(\mathbf{r}_1, \mathbf{r}', \omega) \vec{j}(\mathbf{r}', \omega)] \otimes [\vec{G}(\mathbf{r}_2, \mathbf{r}'', \omega') \vec{j}(\mathbf{r}'', \omega')]^* \rangle \\ &= \omega^2 \mu_0^2 \int_V d^3\mathbf{r}' \int_V d^3\mathbf{r}'' \vec{G}(\mathbf{r}_1, \mathbf{r}', \omega) \langle \vec{j}(\mathbf{r}', \omega) \otimes \vec{j}^*(\mathbf{r}'', \omega') \rangle \vec{G}^\dagger(\mathbf{r}_2, \mathbf{r}'', \omega'), \end{aligned} \quad (8)$$

and using Eq. (3), we get

$$\begin{aligned} \vec{W}(\mathbf{r}_1, \mathbf{r}_2, \omega) &= 4\pi\omega^3 \mu_0^2 \varepsilon_0 \varepsilon''(\omega) \Theta(\omega, T) \\ &\times \int_V d^3\mathbf{r}' \vec{G}(\mathbf{r}_1, \mathbf{r}', \omega) \vec{G}^\dagger(\mathbf{r}_2, \mathbf{r}', \omega). \end{aligned} \quad (9)$$

Thus to compute  $\vec{W}(\mathbf{r}_1, \mathbf{r}_2, \omega)$ , we need to obtain the expression for  $\vec{G}(\mathbf{r}, \mathbf{r}', \omega)$ , which is described below.

Due to the homogeneity of the slab in the  $x$  and  $y$  directions,  $\vec{G}(\mathbf{r}, \mathbf{r}', \omega)$  can be written as

$$\vec{G}(\mathbf{r}, \mathbf{r}', \omega) \equiv \vec{G}(\mathbf{R}_1 - \mathbf{R}', z_0, z', \omega), \quad (10)$$

where  $\mathbf{r}=(\mathbf{R}, z>0)$ ,  $\mathbf{r}'=(\mathbf{R}', -a<z'<0)$ , and  $\mathbf{R}=x\hat{x}+y\hat{y}$  is a vector in the  $x$ - $y$  plane. We can then further represent  $\vec{G}(\mathbf{R}_1 - \mathbf{R}', z_0, z', \omega)$  as

$$\vec{G}(\mathbf{R}_1 - \mathbf{R}', z_0, z', \omega) = \int_{-\infty}^{\infty} \frac{d^2\boldsymbol{\beta}}{4\pi^2} \vec{g}(\boldsymbol{\beta}, z_0, z', \omega) e^{i\boldsymbol{\beta} \cdot (\mathbf{R}_1 - \mathbf{R}')}, \quad (11)$$

where  $\boldsymbol{\beta}$  is a two-dimensional real wave vector in the  $x$ - $y$  plane. Here for simplicity we assume that  $z_1=z_2 \equiv z_0$ . By inserting Eq. (11) into Eq. (9), we get

$$\begin{aligned} \vec{W}(\mathbf{r}_1, \mathbf{r}_2, \omega) &= 4\pi\omega^3 \mu_0^2 \varepsilon_0 \varepsilon''(\omega) \Theta(\omega, T) \int_{-a}^0 dz' \int_{-\infty}^{\infty} d^2\mathbf{R}' \\ &\times \int_{-\infty}^{\infty} \frac{d^2\boldsymbol{\beta}_1}{4\pi^2} \int_{-\infty}^{\infty} \frac{d^2\boldsymbol{\beta}_2}{4\pi^2} \vec{g}(\boldsymbol{\beta}_1, z_0, z', \omega) \\ &\times \vec{g}^\dagger(\boldsymbol{\beta}_2, z_0, z', \omega) e^{i\boldsymbol{\beta}_1 \cdot (\mathbf{R}_1 - \mathbf{R}')} e^{-i\boldsymbol{\beta}_2 \cdot (\mathbf{R}_2 - \mathbf{R}')}. \end{aligned} \quad (12)$$

Using

$$\int_{-\infty}^{\infty} d^2\mathbf{R}' e^{i(\boldsymbol{\beta}_1 - \boldsymbol{\beta}_2) \cdot \mathbf{R}'} = 4\pi^2 \delta^2(\boldsymbol{\beta}_1 - \boldsymbol{\beta}_2), \quad (13)$$

we obtain

$$\begin{aligned} \vec{W}(\mathbf{r}_1, \mathbf{r}_2, \omega) &\equiv \vec{W}(\mathbf{R}_1 - \mathbf{R}_2, z_0, \omega) \\ &= 4\pi\omega^3 \mu_0^2 \varepsilon_0 \varepsilon''(\omega) \Theta(\omega, T) \int_{-a}^0 dz' \int_{-\infty}^{\infty} \frac{d^2\boldsymbol{\beta}}{4\pi^2} \\ &\times \vec{g}(\boldsymbol{\beta}, z_0, z', \omega) \vec{g}^\dagger(\boldsymbol{\beta}, z_0, z', \omega) e^{i\boldsymbol{\beta} \cdot (\mathbf{R}_1 - \mathbf{R}_2)}. \end{aligned} \quad (14)$$

Hence, the sources in the slab collectively excite modes of different in-plane wave vector  $\boldsymbol{\beta}$ . These plane waves then interfere and affect the degree of coherence.

From Eq. (14), the cross-spectral density tensor is thus determined from  $\vec{g}(\boldsymbol{\beta}, z_0, z', \omega)$ . In order to evaluate  $\vec{g}(\boldsymbol{\beta}, z_0, z', \omega)$ , it is useful to consider a solution to Maxwell's

equations in a homogeneous medium:  $\vec{E}e^{i\mathbf{k} \cdot \mathbf{r}}$  where  $\mathbf{k} \cdot \mathbf{k} = (n\omega/c)^2$ . Here  $n$  is the refractive index of the medium. Due to the transversality constraint, we have  $\mathbf{k} \cdot \vec{E} = 0$ . Therefore, for a given two-dimensional wave vector  $\boldsymbol{\beta}$ , the three-dimensional wave vector  $\mathbf{k}$  can be written as

$$\mathbf{k} = \begin{pmatrix} \beta_x \\ \beta_y \\ \gamma \end{pmatrix} = \begin{pmatrix} \beta \cos \phi \\ \beta \sin \phi \\ \gamma \end{pmatrix}, \quad (15)$$

where  $\gamma$  is given by

$$\gamma = \sqrt{(n\omega/c)^2 - \beta^2} \quad (16)$$

and  $\beta \equiv |\boldsymbol{\beta}|$ . If  $n$  is real,  $\gamma$  is imaginary when  $\beta > n\omega/c$ , and the wave becomes evanescent in the  $z$  direction.

Also, at a given  $\boldsymbol{\beta}$ , the solution can be either a  $s$ -polarized (TE) or a  $p$ -polarized (TM) wave. The unit polarization vectors for TE and TM modes can be expressed as

$$\hat{\mathbf{s}} \equiv \frac{\hat{\mathbf{z}} \times \mathbf{k}}{\sqrt{(\hat{\mathbf{z}} \times \mathbf{k}) \cdot (\hat{\mathbf{z}} \times \mathbf{k})}} = \frac{1}{\beta} \begin{pmatrix} -\beta_y \\ \beta_x \\ 0 \end{pmatrix} = \begin{pmatrix} -\sin \phi \\ \cos \phi \\ 0 \end{pmatrix}, \quad (17)$$

$$\hat{\mathbf{p}} \equiv \frac{\mathbf{k}}{\sqrt{\mathbf{k} \cdot \mathbf{k}}} \times \hat{\mathbf{s}} = \frac{c}{n\omega} \begin{pmatrix} -\gamma \cos \phi \\ -\gamma \sin \phi \\ \beta \end{pmatrix}. \quad (18)$$

These vectors are normalized according to  $\hat{\mathbf{s}} \cdot \hat{\mathbf{s}} = 1$  and  $\hat{\mathbf{p}} \cdot \hat{\mathbf{p}} = 1$ . Note that  $\hat{\mathbf{s}}$  is real, lies on the  $x$ - $y$  plane, and is medium independent, while  $\hat{\mathbf{p}}$  can be complex and is medium dependent.  $\hat{\mathbf{s}}$  and  $\hat{\mathbf{p}}$  are orthogonal (i.e.,  $\hat{\mathbf{s}} \cdot \hat{\mathbf{p}} = 0$ ) in all media.

Using the vectors  $\hat{\mathbf{s}}$  and  $\hat{\mathbf{p}}$ ,  $\vec{g}(\boldsymbol{\beta}, z_0, z', \omega)$  can be written as [19]

$$\begin{aligned} \vec{g}(\boldsymbol{\beta}, z_0, z', \omega) &= -\frac{i}{2\gamma_{\text{II}}} [T_s(\beta, z', \omega) \hat{\mathbf{s}} \otimes \hat{\mathbf{s}} \\ &+ T_p(\beta, z', \omega) \hat{\mathbf{p}}_{\text{I}} \otimes \hat{\mathbf{p}}_{\text{II}}] e^{i\gamma z_0}, \end{aligned} \quad (19)$$

where  $T_\zeta(\beta, z', \omega)$  ( $\zeta=s, p$ ) is the transmission coefficient of the  $s$ - or  $p$ -polarized field to free space (denoted by subscript I), from the source plane at  $z=z'$  inside the slab (denoted by subscript II), and is given by [19]

$$T_\zeta(\beta, z', \omega) = \frac{t_\zeta(\beta, \omega) [e^{-i\gamma_{\text{II}} z'} + r_\zeta(\beta, \omega) e^{i\gamma_{\text{II}} (2a+z')}]}{1 - [r_\zeta(\beta, \omega)]^2 e^{i2\gamma_{\text{II}} a}}. \quad (20)$$

Here  $t_\zeta(\beta, \omega)$ ,  $r_\zeta(\beta, \omega)$  are, respectively, the Fresnel transmission and reflection coefficients at a single dielectric-air interface,

$$t_s(\beta, \omega) = \frac{2\gamma_{II}}{\gamma_{II} + \gamma_I}, \quad (21)$$

$$r_s(\beta, \omega) = \frac{\gamma_{II} - \gamma_I}{\gamma_{II} + \gamma_I}, \quad (22)$$

$$t_p(\beta, \omega) = \frac{2n_I n_{II} \gamma_{II}}{n_I^2 \gamma_{II} + n_{II}^2 \gamma_I}, \quad (23)$$

$$r_p(\beta, \omega) = \frac{n_I^2 \gamma_{II} - n_{II}^2 \gamma_I}{n_I^2 \gamma_{II} + n_{II}^2 \gamma_I}. \quad (24)$$

$$\begin{aligned} \vec{W}(\mathbf{r}_1, \mathbf{r}_2, \omega) &= 4\pi\omega^3 \mu_0^2 \epsilon_0 \epsilon''(\omega) \Theta(\omega, T) \\ &\times \int_{-\infty}^{\infty} \frac{d^2\boldsymbol{\beta}}{4\pi^2} \frac{e^{i(\gamma_I - \gamma_I^*)z_0} e^{i\boldsymbol{\beta} \cdot (\mathbf{R}_1 - \mathbf{R}_2)}}{4|\gamma_{II}|^2} \\ &\times \int_{-a}^0 dz' [|T_s(\beta, z', \omega)|^2 (\hat{\mathbf{s}} \cdot \hat{\mathbf{s}}) \hat{\mathbf{s}} \otimes \hat{\mathbf{s}} \\ &+ |T_p(\beta, z', \omega)|^2 (\hat{\mathbf{p}}_{II} \cdot \hat{\mathbf{p}}_{II}^*) \hat{\mathbf{p}}_I \otimes \hat{\mathbf{p}}_I^*], \quad (25) \end{aligned}$$

where

$$\hat{\mathbf{s}} \otimes \hat{\mathbf{s}} = \begin{pmatrix} \sin^2 \phi & -\cos \phi \sin \phi & 0 \\ -\cos \phi \sin \phi & \cos^2 \phi & 0 \\ 0 & 0 & 0 \end{pmatrix} \quad (26)$$

Thus Eq. (14) can be reexpressed as

(note that  $\hat{\mathbf{s}}$  vector is the same in both media),

$$\hat{\mathbf{p}}_I \cdot \hat{\mathbf{p}}_I^* = \left(\frac{c}{\omega}\right)^2 \left(\frac{\beta^2 + |\gamma_I|^2}{|n_I|^2}\right) \geq 1, \quad (27)$$

$$\hat{\mathbf{p}}_I \otimes \hat{\mathbf{p}}_I^* = \left(\frac{c}{\omega}\right)^2 \frac{1}{|n_I|^2} \begin{pmatrix} |\gamma_I|^2 \cos^2 \phi & |\gamma_I|^2 \cos \phi \sin \phi & -\gamma_I \beta \cos \phi \\ |\gamma_I|^2 \cos \phi \sin \phi & |\gamma_I|^2 \sin^2 \phi & -\gamma_I \beta \sin \phi \\ -\gamma_I^* \beta \cos \phi & -\gamma_I^* \beta \sin \phi & \beta^2 \end{pmatrix}, \quad (28)$$

for  $i=I, II$ .

As a further simplification, we can express Eq. (25) in polar coordinates,  $\boldsymbol{\beta}=(\beta, \phi)$ . Without loss of generality, we choose our coordinates such that the two points are aligned on the  $x$  axis, i.e.,  $\mathbf{r}_1=(x, 0, z_0)$ ,  $\mathbf{r}_2=(0, 0, z_0)$ , as in Fig. 1. Then

$$\begin{aligned} \vec{W}(x, z_0, \omega) &= 4\pi\omega^3 \mu_0^2 \epsilon_0 \epsilon''(\omega) \Theta(\omega, T) \int_0^\infty \frac{\beta d\beta}{2\pi} \int_0^{2\pi} \frac{d\phi}{2\pi} \frac{e^{i(\gamma_I - \gamma_I^*)z_0} e^{i\beta x \cos \phi}}{4|\gamma_{II}|^2} \\ &\times \int_{-a}^0 dz' \left[ |T_s(\beta, z', \omega)|^2 \begin{pmatrix} \sin^2 \phi & -\sin \phi \cos \phi & 0 \\ -\sin \phi \cos \phi & \cos^2 \phi & 0 \\ 0 & 0 & 0 \end{pmatrix} \right. \\ &\left. + |T_p(\beta, z', \omega)|^2 \left(\frac{c}{\omega}\right)^4 \left(\frac{\beta^2 + |\gamma_{II}|^2}{|n_{II}|^2}\right) \begin{pmatrix} |\gamma_I|^2 \cos^2 \phi & |\gamma_I|^2 \cos \phi \sin \phi & -\gamma_I \beta \cos \phi \\ |\gamma_I|^2 \cos \phi \sin \phi & |\gamma_I|^2 \sin^2 \phi & -\gamma_I \beta \sin \phi \\ -\gamma_I^* \beta \cos \phi & -\gamma_I^* \beta \sin \phi & \beta^2 \end{pmatrix} \right]. \quad (29) \end{aligned}$$

All off-diagonal elements of  $\vec{W}(x, z_0, \omega)$  in Eq. (29) are zero after the integration over  $\phi$ . Hence  $\vec{W}(x, z_0, \omega)$  is diagonal with our choice of coordinate axes. Therefore, for electric fields of two points displaced along the  $x$  axis, only field components of the same direction correlate.

The diagonal elements of  $\vec{W}(x, z_0, \omega)$  are evaluated to be

$$\begin{aligned} W_{XX}(x, z_0, \omega) &= 4\pi\omega^3 \mu_0^2 \epsilon_0 \epsilon''(\omega) \Theta(\omega, T) \int_0^\infty \frac{\beta d\beta}{2\pi} \frac{e^{i(\gamma_I - \gamma_I^*)z_0}}{4|\gamma_{II}|^2} \int_{-a}^0 dz' \left[ |T_s(\beta, z', \omega)|^2 \frac{J_1(\beta x)}{\beta x} \right. \\ &\left. + |T_p(\beta, z', \omega)|^2 \left(\frac{c}{\omega}\right)^4 \left(\frac{\beta^2 + |\gamma_{II}|^2}{|n_{II}|^2}\right) |\gamma_I|^2 \left( J_0(\beta x) - \frac{J_1(\beta x)}{\beta x} \right) \right], \quad (30) \end{aligned}$$

$$\begin{aligned}
 W_{YY}(x, z_0, \omega) &= 4\pi\omega^3\mu_0^2\varepsilon_0\varepsilon''(\omega)\Theta(\omega, T) \int_0^\infty \frac{\beta d\beta}{2\pi} \frac{e^{i(\gamma_1 - \gamma_1^*)z_0}}{4|\gamma_{II}|^2} \\
 &\times \int_{-a}^0 dz' \left[ |T_s(\beta, z', \omega)|^2 \left( J_0(\beta x) - \frac{J_1(\beta x)}{\beta x} \right) \right. \\
 &\left. + |T_p(\beta, z', \omega)|^2 \left( \frac{c}{\omega} \right)^4 \left( \frac{\beta^2 + |\gamma_{II}|^2}{|n_{II}|^2} \right) |\gamma_I|^2 \frac{J_1(\beta x)}{\beta x} \right], \quad (31)
 \end{aligned}$$

$$\begin{aligned}
 W_{ZZ}(x, z_0, \omega) &= 4\pi\omega^3\mu_0^2\varepsilon_0\varepsilon''(\omega)\Theta(\omega, T) \\
 &\times \int_0^\infty \frac{\beta d\beta}{2\pi} \frac{e^{i(\gamma_1 - \gamma_1^*)z_0}}{4|\gamma_{II}|^2} \int_{-a}^0 dz' \\
 &\times |T_p(\beta, z', \omega)|^2 \left( \frac{c}{\omega} \right)^4 \left( \frac{\beta^2 + |\gamma_{II}|^2}{|n_{II}|^2} \right) \beta^2 J_0(\beta x). \quad (32)
 \end{aligned}$$

To obtain the above expressions, we have used the following identities:

$$\int_0^{2\pi} \frac{d\phi}{2\pi} e^{i\beta x \cos \phi} = J_0(\beta x), \quad (33)$$

$$\int_0^{2\pi} \frac{d\phi}{2\pi} e^{i\beta x \cos \phi} \cos^2 \phi = J_0(\beta x) - \frac{J_1(\beta x)}{\beta x}, \quad (34)$$

$$\int_0^{2\pi} \frac{d\phi}{2\pi} e^{i\beta x \cos \phi} \sin^2 \phi = \frac{J_1(\beta x)}{\beta x}, \quad (35)$$

where  $J_0$  and  $J_1$  are the zeroth- and first-order Bessel functions of the first kind, respectively.

The cross-spectral density tensor can also be expressed by the angular spectrum expansion [16,20]

$$\begin{aligned}
 \vec{\vec{W}}(x, z_0, \omega) &\equiv \int_{-\infty}^\infty \frac{d^2\beta}{4\pi^2} \vec{\vec{W}}(\beta, z_0, \omega) e^{i\beta x \cos \phi} \\
 &= \int_0^\infty \frac{d\beta}{2\pi} \beta \int_0^{2\pi} \frac{d\phi}{2\pi} e^{i\beta x \cos \phi} [\vec{\vec{W}}(\beta, \phi, z_0, \omega)]. \quad (36)
 \end{aligned}$$

$\vec{\vec{W}}$  is the two-dimensional Fourier transform of  $\vec{\vec{W}}$ . This expansion, as we will show below, gives considerable physical insights to the underlying physical mechanisms that determine the coherence behavior.

From Eqs. (32) and (33),  $\vec{\vec{W}}_{ZZ}(\beta, z_0, \omega)$  can be derived as

$$\begin{aligned}
 \vec{\vec{W}}_{ZZ}(\beta, z_0, \omega) &= 4\pi\omega^3\mu_0^2\varepsilon_0\varepsilon''(\omega)\Theta(\omega, T) \frac{e^{i(\gamma_1 - \gamma_1^*)z_0}}{4|\gamma_{II}|^2} \\
 &\times \int_{-a}^0 dz' \left[ |T_p(\beta, z', \omega)|^2 \left( \frac{c}{\omega} \right)^4 \left( \frac{\beta^2 + |\gamma_{II}|^2}{|n_{II}|^2} \right) \beta^2 \right], \quad (37)
 \end{aligned}$$

which is independent of  $\phi$ . On the other hand,  $\vec{\vec{W}}_{XX}$  and  $\vec{\vec{W}}_{YY}$  vary with  $\phi$  in the following manner:

$$\begin{aligned}
 \vec{\vec{W}}_{XX}(\beta, \phi, z_0, \omega) &\propto \sin^2 \phi |T_s(\beta, z_0, \omega)|^2 \\
 &+ \cos^2 \phi |T_p(\beta, z_0, \omega)|^2 \left( \frac{c}{\omega} \right)^4 \frac{\beta^2 + |\gamma_{II}|^2}{|n_{II}|^2} |\gamma_I|^2, \quad (38)
 \end{aligned}$$

$$\begin{aligned}
 \vec{\vec{W}}_{YY}(\beta, \phi, z_0, \omega) &\propto \cos^2 \phi |T_s(\beta, z_0, \omega)|^2 \\
 &+ \sin^2 \phi |T_p(\beta, z_0, \omega)|^2 \left( \frac{c}{\omega} \right)^4 \frac{\beta^2 + |\gamma_{II}|^2}{|n_{II}|^2} |\gamma_I|^2. \quad (39)
 \end{aligned}$$

The sum of  $\vec{\vec{W}}_{XX}$  and  $\vec{\vec{W}}_{YY}$  is  $\phi$  independent,

$$\begin{aligned}
 \vec{\vec{W}}_{XX}(\beta, \phi, z_0, \omega) + \vec{\vec{W}}_{YY}(\beta, \phi, z_0, \omega) &= 4\pi\omega^3\mu_0^2\varepsilon_0\varepsilon''(\omega)\Theta(\omega, T) \frac{e^{i(\gamma_1 - \gamma_1^*)z_0}}{4|\gamma_{II}|^2} \int_{-a}^0 dz' \left[ |T_s(\beta, z', \omega)|^2 \right. \\
 &\left. + |T_p(\beta, z', \omega)|^2 \left( \frac{c}{\omega} \right)^4 \left( \frac{\beta^2 + |\gamma_{II}|^2}{|n_{II}|^2} \right) |\gamma_I|^2 \right]. \quad (40)
 \end{aligned}$$

Finally we define the coherence length as follows:

$$\begin{aligned}
 \xi(z_0, \omega) &\equiv \frac{2 \int_0^\infty dx |\text{Tr}[\vec{\vec{W}}(x, z_0, \omega)]|^2}{|\text{Tr}[\vec{\vec{W}}(x=0, z_0, \omega)]|^2} \\
 &= \frac{2 \int_0^\infty \frac{d\beta_x}{2\pi} \left| \int_{-\infty}^\infty \frac{d\beta_y}{2\pi} \text{Tr}[\vec{\vec{W}}(\beta_x, \beta_y, z_0, \omega)] \right|^2}{\left| \int_0^\infty \frac{\beta d\beta}{2\pi} \text{Tr}[\vec{\vec{W}}(\beta, z_0, \omega)] \right|^2} \\
 &= \frac{2 \int_0^\infty \frac{d\beta_x}{2\pi} \left| 2 \int_{\beta_x}^\infty \frac{d\beta}{2\pi} \frac{\beta}{\sqrt{\beta^2 - \beta_x^2}} \text{Tr}[\vec{\vec{W}}(\beta, z_0, \omega)] \right|^2}{\left| \int_0^\infty \frac{\beta d\beta}{2\pi} \text{Tr}[\vec{\vec{W}}(\beta, z_0, \omega)] \right|^2}, \quad (41)
 \end{aligned}$$

where  $\beta = \sqrt{\beta_x^2 + \beta_y^2}$ ,  $\text{Tr}(\vec{\vec{W}}) = W_{XX} + W_{YY} + W_{ZZ}$ , and  $\text{Tr}(\vec{\vec{W}}) = \vec{\vec{W}}_{XX} + \vec{\vec{W}}_{YY} + \vec{\vec{W}}_{ZZ}$ .

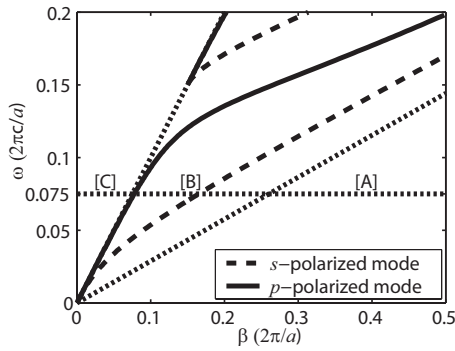


FIG. 2. Dispersion relationship of a lossless dielectric slab with thickness  $a$ , and refractive index  $n=3.4641$ .  $\beta$  is the magnitude of the in-plane wave vector  $\boldsymbol{\beta}$ . In the diagram, we plot the lowest two modes of the  $s$  and  $p$  polarizations. The line  $\omega=0.075(2\pi c/a)$  is the operating frequency. The guided modes of the slab are bounded by the light line of air  $\omega/c=\beta$ , and the light line of the slab  $\omega/c=\beta/n$ . The two light lines are denoted by the dotted lines. We split this diagram into three regions bounded by these light lines. Region [A] refers to the phase space with  $\beta>n\omega/c$ , where waves are evanescent both in the slab and in air along the direction normal to the plane. Region [B] refers to the phase space with  $\omega/c<\beta<n\omega/c$ , where waves are evanescent in air but propagating in the slab in the direction normal to the plane. Region [C] is where  $\beta<\omega/c$  in which waves are propagating in the normal direction both in the slab and in air.

### III. RESULTS AND INTERPRETATIONS

#### A. Spatial coherence at various separations from the slab

We now use the formalism developed in Sec. II to investigate the coherence properties for the slab geometry. We are interested in the case where the absorption in the slab is small, since in this case the guided modes attenuate slowly. As we will show in the following, these guided modes play a significant role in the coherence properties of the thermal fields. The dielectric constant of the slab is chosen as 12

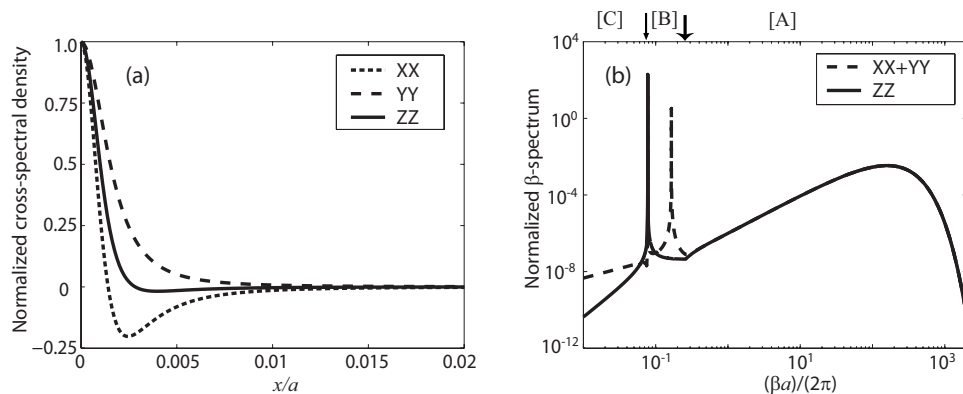


FIG. 3. (a) Components of the normalized cross-spectral density tensor  $W_{mn}(x, z_0, \omega)/W_{nn}(x=0, z_0, \omega)|_{n=X,Y,Z}$  of the dielectric slab in Fig. 1, as defined in Eqs. (30)–(32) at  $z_0=0.001a$  from the slab surface with  $\omega=0.075(2\pi c/a)$ . (b) Corresponding normalized  $\beta$  spectra for the in-plane ( $XX+YY$ ) and  $ZZ$  field components,  $\beta[\tilde{W}_{XX}(\beta, \phi, z_0, \omega) + \tilde{W}_{YY}(\beta, \phi, z_0, \omega)]/[W_{XX}(x=0, z_0, \omega) + W_{YY}(x=0, z_0, \omega)]$  and  $\beta\tilde{W}_{ZZ}(\beta, z_0, \omega)/W_{ZZ}(x=0, z_0, \omega)$ , as defined in Eq. (40) and Eq. (37). Note that  $W_{XX}$  and  $W_{YY}$  are equal at  $x=0$  and the sum  $\tilde{W}_{XX} + \tilde{W}_{YY}$  is independent of  $\phi$ . For each of the  $\beta$ -spectral curves  $f(\beta)$ , the integrated area underneath the curve, i.e.,  $\int_0^\infty \frac{d\beta}{2\pi} f(\beta)$ , is 1. The  $\beta$ -space is divided in the same manner as in Fig. 2 with region [A],  $\beta>\text{Re}(n_{\text{II}})\omega/c$ ; region [B],  $\omega/c<\beta<\text{Re}(n_{\text{II}})\omega/c$ ; and region [C],  $\beta<\omega/c$ , where  $n_{\text{II}}^2$  is the complex dielectric constant of the slab. The arrows denote the boundaries of the regions.

+0.001*i*, which approximates that of heavily doped silicon [21]. The slab is assumed to be in air with dielectric constant of 1.

In Fig. 2 we show the dispersion relation of a lossless slab for both polarizations. The horizontal line indicates the frequency  $\omega=0.075(2\pi c/a)$ , where most of the calculations in this paper are taken. At this frequency, the slab is single moded for both polarizations. For the guided modes, the fields outside the slab (in air) are evanescent away from the slab, with a decay length  $[d_\zeta=1/i\gamma_\zeta=1/\sqrt{\beta_\zeta^2-(\omega/c)^2}]$ , where  $\zeta=s,p$ ] of  $6.81a$  for the  $s$ -polarized mode, and  $49.25a$  for the  $p$ -polarized mode.

The thermal fields at  $z_0$  contain contributions from waves that are either propagating or evanescent in the direction normal to the slab surface. To highlight the contributions from different wave components, with reference to Eq. (29),  $\vec{W}(x, z_0, \omega)$  can be written in the following form with integration range separated into  $\beta \in [\text{Re}(n_{\text{II}})\omega/c, \infty)$ ,  $\beta \in [\omega/c, \text{Re}(n_{\text{II}})\omega/c]$ , and  $\beta \in [0, \omega/c]$ ,

$$\begin{aligned} \vec{W}(x, z_0, \omega) = & \left[ \left( \int_{\text{Re}(n_{\text{II}})\omega/c}^{\infty} + \int_{\omega/c}^{\text{Re}(n_{\text{II}})\omega/c} \right) \right. \\ & \left. \times \frac{\beta d\beta}{2\pi} e^{i(\gamma_{\text{II}} - \gamma_{\text{I}}^*)z_0} e^{i\beta x \cos \phi(\dots)} \right] \\ & + \int_0^{\omega/c} \frac{\beta d\beta}{2\pi} e^{i\beta x \cos \phi(\dots)} = (\vec{W}^{[A]} + \vec{W}^{[B]}) + \vec{W}^{[C]}. \end{aligned} \quad (42)$$

In Eq. (42), the first and second terms are both exponentially decaying functions of  $z_0$ . The first term  $\vec{W}^{[A]}$ , with the range of integration  $\beta \in [\text{Re}(n_{\text{II}})\omega/c, \infty)$ , describes contributions from waves that are evanescent both inside and outside the slab. This term is significant only when  $z_0$  is very close to zero. Below, we refer to such a regime as the “extreme near

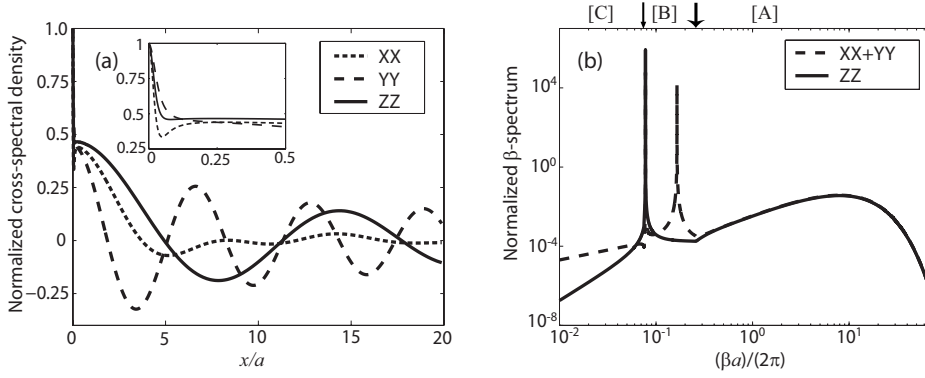


FIG. 4. Same as Fig. 3, except  $z_0 = 0.02a$ . The inset in (a) highlights the region  $0 < x < 0.5a$ .

field.” In this range of  $\beta$ , the integrand in Eq. (42) appears as a broadband spectrum of  $\beta$  with local maximum located at a large  $\beta$  value. This gives rise to a narrow peak in  $\vec{W}(x, z_0, \omega)$  around  $x=0$  and a very short coherence length. In the second term  $\vec{W}^{[B]}$ ,  $\beta \in [\omega/c, \text{Re}(n_{II})\omega/c]$  covers the wavenumber range where guided modes exist. In this range, the waves are propagating inside the slab. The wavenumber  $\beta$  of the guided modes manifests as poles in the transmission coefficients  $|T_{\zeta=s,p}(\beta, z', \omega)|^2$ . These poles result in the oscillatory behavior of  $\vec{W}(x, z_0, \omega)$  as a function of  $x$ , when  $z_0$  is comparable to the evanescent decay lengths of the guided modes. We refer to this regime as the “intermediate near-field” regime. The third term  $\vec{W}^{[C]}$  is independent of  $z_0$ , as  $\gamma_1$  is real for  $\beta \in [0, \omega/c]$ . This term represents the contribution from propagating waves and dominates in the far field. The classification of the extreme near-, intermediate near-, and far-field regimes by relative dominance in the  $\beta$  spectrum is consistent with our definition in Sec. I based on comparing  $z_0$  with the decay lengths of waveguide modes.

In Figs. 3–6, we plot all components of the normalized cross-spectral density tensor  $W_{mn}(x, z_0, \omega)/W_{mn}(x=0, z_0, \omega)|_{n=X,Y,Z}$  at various  $z_0$ ,  $z_0 = 0.001a, 0.02a, 1a, 200a$ , where  $z_0 = 0.001a \ll d$  belongs to the extreme near-field zone;  $z_0 = 200a \gg d$  belongs to the far field; while  $z_0 = 0.02a$  and  $z_0 = 1a$  are at the intermediate near-field zone. The normalized  $\beta$  spectra,  $\beta[\vec{W}_{XX}(\beta, \phi, z_0, \omega) + \vec{W}_{YY}(\beta, \phi, z_0, \omega)]/[W_{XX}(x=0, z_0, \omega) + W_{YY}(x=0, z_0, \omega)]$  and  $\beta\vec{W}_{ZZ}(\beta, z_0, \omega)/W_{ZZ}(x=0, z_0, \omega)$ , are also plotted. For each of the  $\beta$ -spectral curves  $f(\beta)$ , the integrated area underneath the curve, i.e.,  $\int_0^\infty \frac{d\beta}{2\pi} f(\beta)$ , is 1.

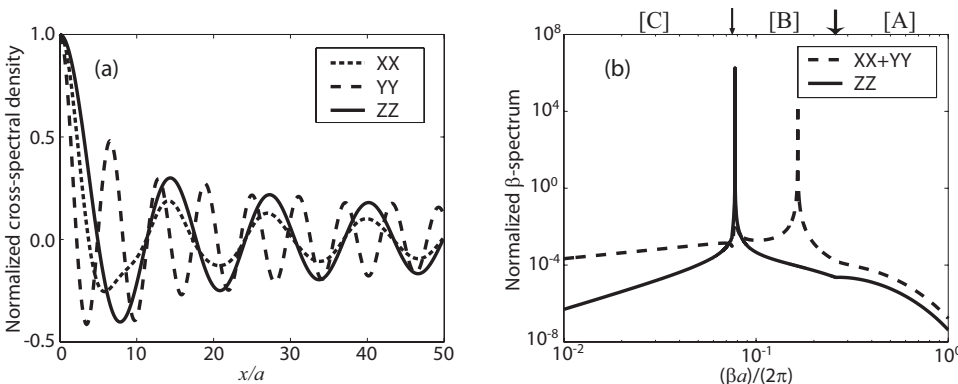


FIG. 5. Same as Fig. 3, except  $z_0 = 1a$ .

Figure 3(a) shows  $\vec{W}(x, z_0, \omega)$  as a function of  $x$ , at  $z_0 = 0.001a$  which amounts to  $7.5 \times 10^{-5}\lambda$  when  $\omega = 0.075(2\pi c/a)$ . It is clearly seen that, in this extreme near-field zone,  $\vec{W}^{[A]}$  dominates and the degree of coherence decreases rapidly with  $x$  for all  $W_{XX}$ ,  $W_{YY}$ , and  $W_{ZZ}$ . The coherence length, as defined in Eq. (41) is  $\xi = 1.51 \times 10^{-3}a = 1.13 \times 10^{-4}\lambda \sim z_0$ . This is much smaller than the thickness of the slab and the skin depth of the material. {The skin depth  $\lambda/[2\pi \text{Im}(n_{II})]$  is equal to  $1.47 \times 10^4 a$  for our operating wavelength and is the  $1/e$  amplitude decay length in the uniform material.}

The extremely short coherence length here reflects the domination of the first term in Eq. (42). In Fig. 3(b), we plot  $\beta\vec{W}(\beta, z_0, \omega)$  as a function of  $\beta$ . The integral of  $\beta\vec{W}(\beta, z_0, \omega)$  with respect to  $\beta$  is clearly dominated by region [A]. In addition, the extent of this integrated area can be characterized by the local maximum of  $\beta\vec{W}(\beta, z_0, \omega)$  in the range  $\beta \in [\text{Re}(n_{II})\omega/c, \infty)$ , which is approximately at  $\beta \approx 3/(2z_0)$  as shown in the Appendix. Therefore, the smaller  $z_0$  is, the larger the contribution from  $\vec{W}^{[A]}$  and the smaller the coherence length  $\xi$ .

Physically, the short range of coherence in the extreme near field can be understood as follows: For  $p$ -polarized field, the electric field has a  $z$ -component that is perpendicular to the dielectric-air interfaces. Due to the dielectric constant discontinuity at these interfaces, there are thermally induced fluctuating charges at the interface. Since the electric field diverges in the vicinity of a point charge, the coherence length becomes very small for the electric field. For  $s$ -polarized field, the electric field is parallel to the interface and there is no corresponding charge at the interface. Hence

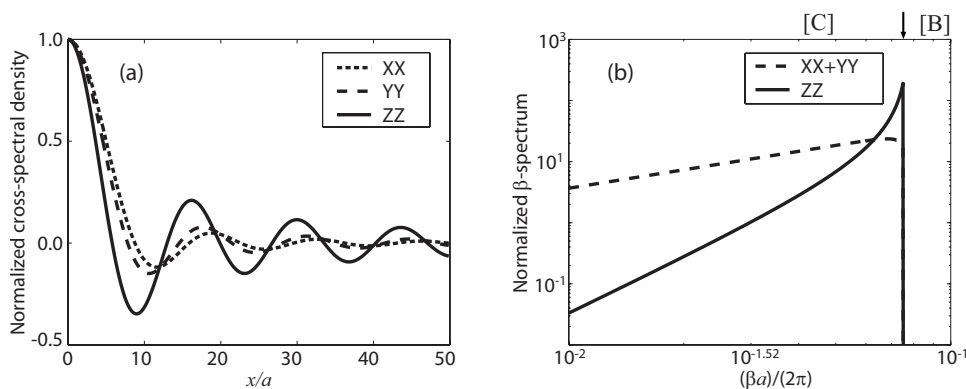


FIG. 6. Same as Fig. 3, except  $z_0=200a$ , and in (b) region [A] is not shown.

the coherence length does not approach zero in the extreme near field for the purely  $s$ -polarized field.  $W_{XX}$ ,  $W_{YY}$ , and  $W_{ZZ}$ , however, all have contributions from the  $p$ -polarized field [Eqs. (25)–(28)], and hence all have very small coherence length in this regime. For magnetic field, similar reasoning leads to vanishing coherence length in the extreme near-field zone for the  $s$  polarization, since, in such a case, there is a fluctuating current in the surface.

Figure 4(a) shows  $\vec{W}(x, z_0, \omega)$  at  $z_0=0.02a$ , which amounts to  $1.5 \times 10^{-3}\lambda$  at  $\omega=0.075(2\pi c/a)$ . In this case, both  $\vec{W}^{[A]}$  and  $\vec{W}^{[B]}$  contribute significantly. As shown in Fig. 4(b), the areas under the curves of  $\beta\vec{W}_{mm}(\beta, z_0, \omega)$  in the range  $\beta \in [\text{Re}(n_{II})\omega/c, \infty)$  and  $\beta \in [\omega/c, \text{Re}(n_{II})\omega/c]$  are of the same order. As a result,  $\vec{W}(x, z_0, \omega)$  shows both features: a narrow peak for small  $x$  due to  $\vec{W}^{[A]}$  and an oscillating behavior for larger  $x$  attributed to  $\vec{W}^{[B]}$ . A kink shows up where the narrow peak connects to the oscillatory part. The coherence pattern is therefore characterized by two length scales: one characterizes the width of the narrow peak, and another one characterizes the decaying oscillatory behavior.

Figure 5(a) shows  $\vec{W}(x, z_0, \omega)$  as a function of  $x$  at  $z_0=1a$ , which amounts to  $7.5 \times 10^{-2}\lambda$  at  $\omega=0.075(2\pi c/a)$ . This is consistent with Fig. 5(b), which shows that  $\vec{W}^{[B]}$ , i.e., the area under the curves  $\beta\vec{W}(\beta, z_0, \omega)$  in the range  $\beta \in [\omega/c, \text{Re}(n_{II})\omega/c]$ , dominates the integral in Eq. (42). The coherence length,  $\xi=17.87a=1.34\lambda$ , as calculated from Eq. (41), is longer than  $\lambda/2$  of the blackbody [22]. Such enhancement of coherence is due to the slab waveguide modes, as indicated by the dominance of  $\vec{W}^{[B]}$ . Also shown in Fig. 5(a) is that coherence enhancement occurs in all field components, though with a varying degree. This is distinct from the polaritonic-induced coherence enhancement which occurs only for field components in the  $x$ - $z$  plane [10].

In this regime, nevertheless, all components of the cross-spectral density tensor still decay as a function of  $x$  because of the following two factors:

(1) In the range  $\beta \in [\omega/c, \text{Re}(n_{II})\omega/c]$ , guided modes determine the location of the poles of  $|T_s(\beta, z', \omega)|^2$  and  $|T_p(\beta, z', \omega)|^2$ . These resonance peaks result in the long-ranged oscillatory behavior in the cross-spectral density tensor. When loss is present in the slab, however, these peaks gain finite width and the range of coherence is thus limited.

(2) The second factor for the decay is in fact purely geometrical due to the three-dimensional nature of the problem,

and is therefore independent of the loss. In the case where loss in the waveguide is very small, at the lowest order,  $\int_{-a}^0 dz' |T_s(\beta, z', \omega)|^2$  and  $\int_{-a}^0 dz' |T_p(\beta, z', \omega)|^2$  can be approximated as  $\int_{-a}^0 dz' |T_s(\beta, z', \omega)|^2 \sim a_s \delta(\beta - \beta_s)$  and  $\int_{-a}^0 dz' |T_p(\beta, z', \omega)|^2 \sim a_p \delta(\beta - \beta_p)$  with  $0 < a_p, a_s < 1$ .  $a_s$  and  $a_p$  are proportional to the area of the bounded regions by the curve  $\vec{W}_{XX} + \vec{W}_{YY}$  around the  $s$  and  $p$  poles. Hence from Eqs. (30)–(32), the components of the cross-spectral density tensor take the following forms:

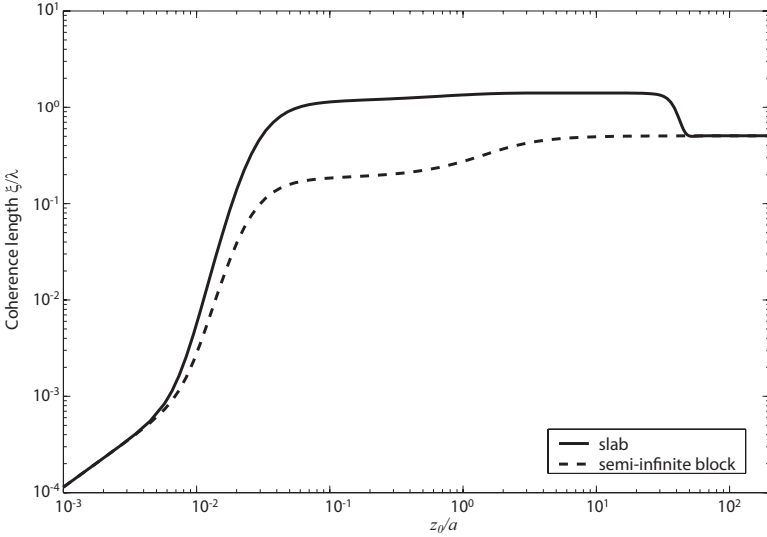
$$W_{XX}(x, z_0, \omega)|_{\text{Im}(n_{II}) \rightarrow 0} = f_{XX}(z_0, \omega) \left[ a_s(z_0, \omega) \frac{J_1(\beta_s x)}{\beta_s x} + a_p(z_0, \omega) \left( J_0(\beta_p x) - \frac{J_1(\beta_p x)}{\beta_p x} \right) \right], \quad (43)$$

$$W_{YY}(x, z_0, \omega)|_{\text{Im}(n_{II}) \rightarrow 0} = f_{YY}(z_0, \omega) \left[ a_s(z_0, \omega) \left( J_0(\beta_s x) - \frac{J_1(\beta_s x)}{\beta_s x} \right) + a_p(z_0, \omega) \frac{J_1(\beta_p x)}{\beta_p x} \right], \quad (44)$$

$$W_{ZZ}(x, z_0, \omega)|_{\text{Im}(n_{II}) \rightarrow 0} = f_{ZZ}(z_0, \omega) J_0(\beta_p x), \quad (45)$$

where  $f_{XX}(z_0, \omega) = f_{YY}(z_0, \omega)$ . Since both  $J_0(\beta x)$  and  $J_1(\beta x)/(\beta x)$  decrease as a function of  $x$ , the components of the cross-spectral density tensor decrease with  $x$  even when loss is infinitesimal. Moreover, since from Eqs. (43)–(45),  $\text{Tr}[\vec{W}(x)] = W_{XX}(x) + W_{YY}(x) + W_{ZZ}(x) = f_{XX} a_s J_0(\beta_s x) + (f_{XX} a_p + f_{ZZ}) J_0(\beta_p x)$ , we see that the envelope of the trace of the cross-spectral density tensor decays asymptotically as  $1/\sqrt{x}$  when the loss is small.

Figures 6(a) and 6(b) show  $\vec{W}(x, z_0, \omega)$  at  $z_0=200a(=15\lambda)$ . At this far-field zone, all contributions from evanescent waves (i.e.,  $\beta > \omega/c$ ) become negligible. Only the radiative components from region [C] (i.e.,  $\beta < \omega/c$ ) survive, as seen from Fig. 6(b). The coherence length as calculated from Eq. (41) is  $\xi=0.503\lambda$ , which is close to the blackbody value [22], and is smaller than that in the intermediate near-field zone. The envelope of the trace of the cross-spectral density tensor also decays approximately as  $1/x$ , which is similar to the behavior of a blackbody [22].



In Fig. 7, we plot the coherence length as a function of  $z_0$  at  $\omega=0.075(2\pi c/a)$ , which summarizes the coherence properties of the system. For comparison purposes, the case of a semi-infinite block with the same dielectric constant is also plotted. At far-field and the extreme near-field zones, the coherence lengths for the two cases almost coincide. The contribution of the waveguide modes is only prominent in the intermediate near-field zone. For  $\varepsilon''=10^{-3}$ , the maximum coherence length is  $1.4\lambda$  at  $z_0=6.3a$ .

### B. Local energy spectral density at constant separation from the slab

The trace of the cross-spectral density tensor at  $x=0$  is proportional to the local energy spectral density  $I(z_0, \omega)$ ,

$$I(z_0, \omega) \equiv \frac{\varepsilon_0}{2\pi^2} \text{Tr}[\vec{W}(x=0, z_0, \omega)] = \frac{1}{2} \frac{\omega^2}{\pi^2 c^3} \Theta(\omega, T) \times \left\{ \frac{4\pi\omega\varepsilon''(\omega)}{c} \int_0^\infty \frac{\beta d\beta}{2\pi} \frac{e^{i(\gamma_1 - \gamma_1^*)z_0}}{4|\gamma_{II}|^2} \int_{-a}^0 dz' \times \left[ |T_s(\beta, z', \omega)|^2 + |T_p(\beta, z', \omega)|^2 \right] \times \left( \frac{c}{\omega} \right)^4 \left( \frac{\beta^2 + |\gamma_{II}|^2}{|n_{II}|^2} \right) (\beta^2 + |\gamma_I|^2) \right\}. \quad (46)$$

$I(z_0, \omega)$  is defined such that the energy density at  $z_0$  is  $\int_0^\infty d\omega I(z_0, \omega)$ . The contribution of each field component to the total local energy spectral density can be seen by expressing Eq. (46) as  $I(z_0, \omega) = \frac{\varepsilon_0}{2\pi^2} \sum_{n=X,Y,Z} W_{nn}(x=0, z_0, \omega)$  with  $W_{XX} = W_{YY}$  at  $x=0$ . The quantity  $I(z_0, \omega)$  is of interest, for example, in thermally induced forces between nanodevices, as well as in near-field spectroscopy [23,24]. Below we focus on the behavior of  $I(z_0, \omega)$  as a function of the normalized frequency  $(\omega a)/(2\pi c)$ , at  $z_0=1a$  for our slab structure. As we will see below, the variation of the normalized frequency allows one to span the extreme near-field, intermediate near-field, and the far-field zones, as previously described.

FIG. 7. Coherence length  $\xi(z_0)$  as a function of distance  $z_0$  from the air-dielectric interface. Coherence length is calculated according to Eq. (41) with the operating frequency  $\omega = 0.075(2\pi c/a)$ . The solid line is the case of a slab with thickness  $a$ . The dashed line shows the case of the corresponding semi-infinite block, with all material constants the same as in the slab.

We define the temperature-independent normalized local energy spectral density  $I^{[\text{norm}]}(z_0, \omega)$  as

$$I^{[\text{norm}]}(z_0, \omega) = \frac{I(z_0, \omega)}{\frac{1}{2} \frac{\omega^2}{\pi^2 c^3} \Theta(\omega, T)}, \quad (47)$$

where the normalization factor  $\frac{1}{2} \frac{\omega^2}{\pi^2 c^3} \Theta(\omega, T)$  is equal to the energy spectral density from a semi-infinite blackbody block with dielectric constant  $\varepsilon = \lim_{\varepsilon' \rightarrow 1, \varepsilon'' \rightarrow 0} \varepsilon' + i\varepsilon''$ . (The  $1/2$  factor is due to the fact that the radiation only propagates outward from the blackbody.)  $I^{[\text{norm}]}(z_0, \omega)$  is dimensionless and is less than or equal to one at far field. At near field, it can exceed 1 due to the contributions from evanescent waves [23].

In Fig. 8 we plot the normalized  $\frac{\varepsilon_0}{2\pi^2} W_{ZZ}(x=0, z_0=1a, \omega)$  and  $\frac{\varepsilon_0}{2\pi^2} W_{YY}(x=0, z_0=1a, \omega)$  as a function of  $(\omega a)/(2\pi c)$ . In the intermediate near-field zone  $0.01 \leq (\omega a)/(2\pi c) < 10$ , os-

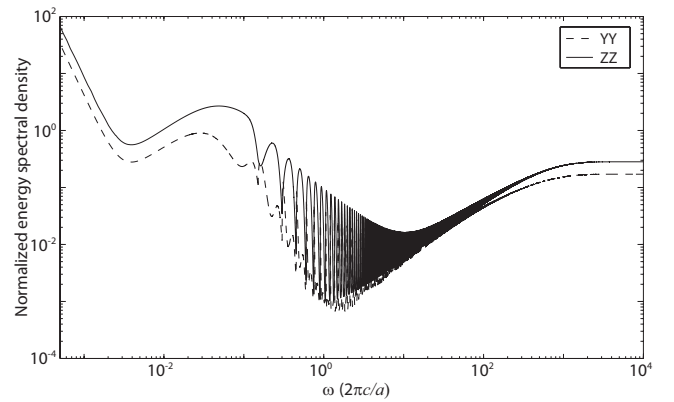


FIG. 8. The plot of  $YY$  and  $ZZ$  contributions to the normalized local energy spectral density  $I^{[\text{norm}]}(z_0, \omega)$  at  $z_0=a$ , as a function of normalized frequency  $\frac{\omega a}{2\pi c}$  in the range  $5 \times 10^{-4} < \frac{\omega a}{2\pi c} < 10^4$  of the slab structure with thickness  $a$ . The dashed line ( $YY$ ) is  $\left[ \frac{\varepsilon_0}{2\pi^2} W_{YY}(x=0, z_0=a, \omega) \right] / \left[ \frac{1}{2} \frac{\omega^2}{\pi^2 c^3} \Theta(\omega, T) \right]$  and the solid line ( $ZZ$ ) is  $\left[ \frac{\varepsilon_0}{2\pi^2} W_{ZZ}(x=0, z_0=a, \omega) \right] / \left[ \frac{1}{2} \frac{\omega^2}{\pi^2 c^3} \Theta(\omega, T) \right]$ .

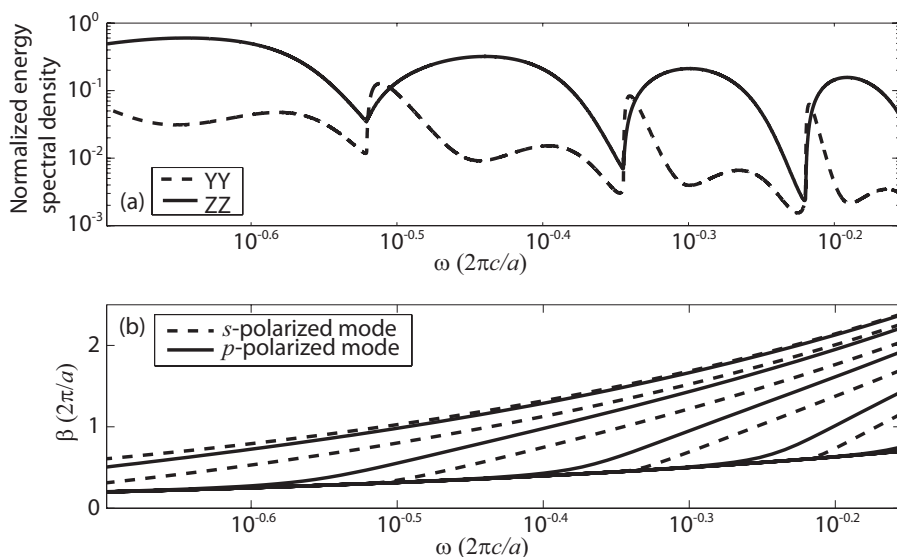


FIG. 9. (a) The  $YY$  and  $ZZ$  contributions to the normalized local energy spectral density  $I^{[\text{norm}]}(z_0, \omega)$  at the range  $0.2 < \frac{\omega a}{2\pi c} < 0.7$  which shows oscillatory patterns. (b) The dispersion relation of the corresponding lossless slab of the same thickness with refractive index  $n = 3.4641$ , plotted at the same frequency range of  $0.2 < \frac{\omega a}{2\pi c} < 0.7$ , to illustrate the correspondence of the fluctuation pattern in (a) with the  $s$ - and  $p$ -waveguide modes.

cillations arise as a function of frequency. The oscillation pattern can be understood by considering the corresponding dispersion relation of the waveguide modes shown in Fig. 9(a) and Fig. 9(b) for the frequency range of  $0.2 < (\omega a)/(2\pi c) < 0.7$ , where oscillation pattern is discernible. For the  $E_y$  field, which is primarily dominated by contributions from the  $s$ -polarized wave (and in fact is completely dominated by the  $s$ -polarized wave at the cutoff), the peaks in energy spectral density coincide with the cutoff frequencies of the  $s$ -polarized waveguide modes, since at the cutoff of each mode the decay length of the guided mode in air is infinitely large. As the operating frequency moves away from the cutoff, the guided mode shifts away from the light line and the vertical decay length decreases. Thus the local energy spectral density drops accordingly until the cutoff of the next-order guided mode appears.

We also note a significant difference in the oscillatory patterns between the  $E_z$  and  $E_y$  contributions to the total energy spectral density. Note that  $E_z$  is totally attributed to the  $p$ -polarized field, while  $E_y$  is related to both  $s$ - and  $p$ -polarized fields. Although the  $s$ - and  $p$ -polarized modes have the same cutoff frequency, in the immediate vicinity above the cutoff frequency, the dispersion relation for the  $p$ -polarized guided modes stays very close to the light line. Hence the energy spectral density from  $E_z$  continues to increase as frequency increases, until the dispersion relation of the  $p$ -polarized guided modes significantly deviates from the light line, and therefore, while the peaks from  $E_y$  are located approximately at the cutoffs, the maxima from  $E_z$  are located away from the cutoffs. We also note that there are secondary maxima for  $E_y$ , with locations that approximately coincide with that of the  $E_z$  field. Such maxima arise from the contribution of the  $p$ -polarized field. Finally, the total energy spectral density spectrum  $I(z_0 = a, \omega) = \frac{\epsilon_0}{2\pi^2} (2W_{YY} + W_{ZZ})$  also oscillates in the intermediate near-field zone with the same oscillation period in frequency.

In the low-frequency limit, when the slab is in the single mode regime, no oscillatory pattern exists and the local energy spectral density increases monotonously at decreasing frequency. This is in fact a signature of the region of extreme near field. As we will prove in the Appendix, at constant frequency, the energy spectral density increases exponentially with decreased vertical separation from a slab at the extreme near-field regime. In the high-frequency limit, the oscillatory pattern gradually disappears as all evanescent components no longer contribute. Only the propagating wave components remain, and there is no vertical intensity variation. In fact, the high-frequency limit of the normalized energy spectral density is determined by the emissivity of the slab.

#### IV. CONCLUSION

In summary, we have derived from first principles the coherence property of the radiative thermal field from a uniform dielectric slab with loss. For a given frequency  $\omega$ , coherence length is extremely short at close proximity from the slab. At a distance of roughly the evanescent length of the waveguide resonances, long-ranged coherence is possible due to slab waveguide modes. At the far-field zone, the coherence length is reduced to approximately  $\lambda/2$ , which is close to the blackbody value [22]. Also, in the case of small loss (for example,  $\epsilon'' = 10^{-3}$  as in this paper), the envelope of the trace of the cross-spectral density tensor decays approximately as  $1/\sqrt{x}$  at the intermediate near field, in contrast to  $\sim 1/x$  in the far field, where  $x$  refers to displacement parallel to the slab surface.

The existence of long-ranged coherence from a dielectric slab is a significant result, since until now, this effect is known to exist only with special type of materials that allow the formation of surface polaritons [10]. In this paper, we show that long-ranged coherence can be achieved for any

dielectric slab. Such long-ranged coherence can be exploited to control the spatial and polarization dependence of the coherence in the far field by introducing grating structures on the surface of the dielectric slab. Furthermore, the strong enhancement of the local energy spectral density in the extreme near field may be useful in thermal photovoltaic applications [4,25].

#### ACKNOWLEDGMENTS

This work is supported in part by DARPA (Grant No. HR0011-05-1-0006), and NSF (Grant No. ECS-0134607).

#### APPENDIX

Here we provide a detailed derivation of the behavior of the cross-spectral density tensor in the extreme near field. The origin of the extreme near-field region can be traced back to the complex nature of the unit vector  $\hat{\mathbf{p}}$ . The scalar product  $\hat{\mathbf{p}} \cdot \hat{\mathbf{p}}^*$ , as in Eq. (27), is larger than unity and diverges at large  $\beta$ . In Eq. (37) or Eq. (40), this divergence dominates the results of integration when  $z_0 \ll \frac{1}{\text{Im}(\gamma)}$ ,  $\frac{1}{\text{Im}(\gamma)}$ .

When  $\beta \gg \text{Re}(n_{\text{II}})\omega/c$ , the terms  $|T_{s,p}(\beta, z_0, \omega)|^2$  are roughly constant, and we can take the following limit:

$$\lim_{\beta \gg \text{Re}(n_{\text{II}})\omega/c} \text{Im}(\sqrt{(n_{\text{II}}\omega/c)^2 - \beta^2}) = \text{Im}(\gamma_{\text{I,II}}) = |\gamma_{\text{I,II}}| = \beta, \quad (\text{A1})$$

with  $n_{\text{I}} = 1$ .

Therefore, by grouping all terms that are either independent, or only slowly varying with  $\beta$  into a single  $\beta$ -independent coefficient, Eq. (37) can be rewritten as

$$\begin{aligned} \beta \tilde{W}_{ZZ}(\beta, z_0, \omega) \Big|_{\beta \gg \text{Re}(n_{\text{II}})\omega/c} &= \text{const} \times \frac{\beta e^{i(\gamma_{\text{I}} - \gamma_{\text{II}})z_0} \left(\frac{c}{\omega}\right)^4 \left(\frac{\beta^2 + |\gamma_{\text{II}}|^2}{|n_{\text{II}}|^2}\right) \beta^2}{|\gamma_{\text{II}}|^2} \\ &= \text{const} \times \frac{\beta e^{-2\beta z_0} \left(\frac{c}{\omega}\right)^4 \left(\frac{2\beta^2}{|n_{\text{II}}|^2}\right) \beta^2}{\beta^2} \\ &= \text{const} \times \left(\frac{c}{\omega}\right)^4 \frac{2}{|n_{\text{II}}|^2} \beta^3 e^{-2\beta z_0}. \end{aligned} \quad (\text{A2})$$

Hence the maximum of  $\beta \tilde{W}_{ZZ}(\beta, z_0, \omega) \Big|_{\beta \gg \text{Re}(n_{\text{II}})\omega/c}$  occurs approximately at

$$\beta_{\text{max}} = \frac{3}{2z_0}. \quad (\text{A3})$$

The same  $\beta_{\text{max}}$  can be obtained for  $\beta [\tilde{W}_{XX} + \tilde{W}_{YY}] \Big|_{\beta \gg \text{Re}(n_{\text{II}})\omega/c}$  from Eq. (40).

As  $z_0$  gets smaller, the broad plateau in the spectral density continuum spans over a wider range in the  $\beta$  spectrum and the coherence length becomes smaller.

- 
- [1] L. Mandel and E. Wolf, *Optical Coherence and Quantum Optics* (Cambridge University Press, Cambridge, England, 1995), p. 369.
- [2] I. Celanovic, D. Perreault, and J. Kassakian, *Phys. Rev. B* **72**, 075127 (2005).
- [3] C. M. Cornelius and J. P. Dowling, *Phys. Rev. A* **59**, 4736 (1999).
- [4] S. Y. Lin, J. Moreno, and J. G. Fleming, *Appl. Phys. Lett.* **83**, 380 (2003).
- [5] C. Luo, A. Narayanaswamy, G. Chen, and J. D. Joannopoulos, *Phys. Rev. Lett.* **93**, 213905 (2004).
- [6] D. L. C. Chan, M. Soljagic, and J. D. Joannopoulos, *Phys. Rev. E* **74**, 036615 (2006).
- [7] D. L. C. Chan, M. Soljagic, and J. D. Joannopoulos, *Opt. Express* **14**, 8785 (2006).
- [8] M. Laroche, R. Carminati, and J.-J. Greffet, *Phys. Rev. Lett.* **96**, 123903 (2006).
- [9] C. Henkel, K. Joulain, R. Carminati, and J.-J. Greffet, *Opt. Commun.* **186**, 57 (2000).
- [10] R. Carminati and J.-J. Greffet, *Phys. Rev. Lett.* **82**, 1660 (1999).
- [11] J.-J. Greffet, R. Carminati, K. Joulain, J.-P. Mulet, S. Mainguy, and Y. Chen, *Nature (London)* **416**, 61 (2002).
- [12] A. V. Shchegrov, K. Joulain, R. Carminati, and J.-J. Greffet, *Phys. Rev. Lett.* **85**, 1548 (2000).
- [13] X.-G. Liang and M.-H. Han, *Chin. Phys. Lett.* **23**, 1219 (2006).
- [14] H. B. Callen and T. A. Welton, *Phys. Rev.* **83**, 34 (1951).
- [15] S. M. Rytov, Yu. A. Kravtsov, and V. I. Tatarskii, *Principles of Statistical Radiophysics 3* (Springer-Verlag, Berlin, 1989), p. 118.
- [16] In this paper the convention of Fourier transform is  $f(x) = \int_{-\infty}^{\infty} \frac{dk}{2\pi} f(k) e^{ikx}$  for spatial domain and  $f(t) = \int_{-\infty}^{\infty} \frac{d\omega}{2\pi} f(\omega) e^{-i\omega t}$  for temporal domain.
- [17] L. Mandel and E. Wolf, *Optical Coherence and Quantum Optics* (Cambridge University Press, Cambridge, England, 1995), p. 363.
- [18] L. Mandel and E. Wolf, *Optical Coherence and Quantum Optics* (Cambridge University Press, Cambridge, England, 1995), p. 59.
- [19] J. E. Sipe, *J. Opt. Soc. Am. B* **4**, 481 (1987).
- [20] L. Mandel and E. Wolf, *Optical Coherence and Quantum Optics* (Cambridge University Press, Cambridge, England, 1995), p. 110.
- [21] R. A. Soref and B. R. Bennett, *IEEE J. Quantum Electron.* **QE-23**, 123 (1987).
- [22] W. H. Carter and E. Wolf, *J. Opt. Soc. Am.* **65**, 1067 (1975).
- [23] K. Joulain, R. Carminati, J.-P. Mulet, and J.-J. Greffet, *Phys. Rev. B* **68**, 245405 (2003).
- [24] Y. D. Wilde *et al.*, *Nature (London)* **444**, 740 (2006).
- [25] A. Narayanaswamy and G. Chen, *Appl. Phys. Lett.* **82**, 3544 (2003).